THE JOURNAL OF PHYSICAL CHEMISTRY B

Article

pubs.acs.org/JPCB

Effects of Protein Conformation, Apparent Solubility, and Protein–Protein Interactions on the Rates and Mechanisms of Aggregation for an IgG1Monoclonal Antibody

Cavan Kalonia,[*,†,‡] Vishal Toprani,[†] Ronald Toth,[†] Newton Wahome,[†,§] Ian Gabel,[†] C. Russell Middaugh,[†] and David B. Volkin[†]

[†]Department of Pharmaceutical Chemistry, Macromolecule and Vaccine Stabilization Center, University of Kansas, Lawrence, Kansas 66047, United States

Supporting Information

ABSTRACT: Non-native protein aggregation is a key degradation pathway of immunoglobulins. In this work, the aggregation kinetics of an immunoglobulin gamma-1 monoclonal antibody (IgG1 mAb) in different solution environments was monitored over a range of incubation temperatures for up to seven months using size exclusion chromatography. Histidine and citrate buffers with/without sodium chloride were employed to modulate the mAb's conformational stability, solubility (in the presence of polyethylene glycol, PEG), and protein–protein interactions as measured by differential scanning calorimetry, PEG precipitation, and static light scattering, respectively. The effect of these parameters on the mechanism(s) of mAb aggregation during storage at different temperatures was determined using kinetic models, which were used to fit aggregation data to determine rate constants for aggregate nucleation and growth processes. This approach was used to investigate the effects of colloidal protein–protein interactions and solubility values (in PEG solutions) on the mechanisms and rates of IgG1 mAb aggregation as a function of temperature-induced structural perturbations. Aggregate nucleation and growth pathways for this IgG1 mAb were sensitive to temperature and overall conformational stability. Aggregate growth, on the other hand, was also sensitive to conditions affecting the solubility of the mAb, particularly at elevated temperatures.

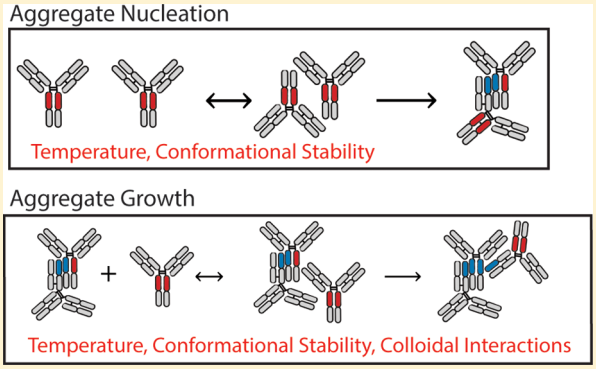

INTRODUCTION

Non-native protein aggregation, or the assembly of proteins into conformationally altered agglomerates, is a multistep process that can occur by different mechanisms through various molecular and colloidal steps.[1−3] In the biopharmaceutical industry, non-native aggregation of therapeutic proteins is a highly undesirable phenomenon because the presence of protein aggregates can compromise drug efficacy by decreasing potency and/or by increasing product immunogenicity potential (i.e., formation of antidrug antibodies).[4−10] The process of non-native, irreversible protein aggregation (hereafter referred to as aggregation) can result in aggregates ranging in size from soluble dimers to insoluble macroscopic particles.[11] The extent of protein aggregation is largely determined by the sequence and structure of the protein itself,[12,13] solution environment (e.g., pH, ionic strength, cosolutes),[14−16] and stress condition applied to induce aggregation (e.g., temperature, mechanical agitation, light, etc.).[17] Recent studies, for example, suggest that mechanical agitation induces aggregation of protein molecules at the air–solution interface[18] whereas incubation at elevated temperatures promotes aggregation of proteins in bulk solution.[19] Cosolutes may affect protein aggregation mechanisms and/or rates by modifying protein conformation, protein structural stability, protein solubility, and/or reversible protein–protein interactions in solution.[20]

Traditionally, protein aggregation has been mechanistically interpreted using the Lumry-Eyring model, in which a reversible conformational change of the protein is followed by an irreversible association step.[21] If aggregation follows the Lumry-Eyring model, the kinetics will be highly sensitive to the fraction of partially unfolded species because of the second order concentration dependence described by the model. For this reason, evaluating measures of protein conformational stability is often used to understand protein aggregation. Differential scanning calorimetry is one technique that is commonly employed for this purpose because it can be used to measure endothermic transitions attributed to protein unfolding as a function of temperature under different solution conditions.

Received: April 16, 2016
Revised: July 3, 2016
Published: July 5, 2016

DOI: 10.1021/acs.jpcb.6b03878
J. Phys. Chem. B 2016, 120, 7062−7075

Contrary to the Lumry-Eyring model, there are examples of native proteins associating prior to undergoing a conformational change to form an aggregate.[21,22] Quantifying the concentration of such transient encounter complexes by direct experimental methods is technically challenging because of the reversible and thermodynamically unstable nature of these intermediates, which may cause them to exist for only a short time in extremely small quantities. In several studies, one approach to address this challenge involved the observation that protein aggregation propensity in different solutions correlated to solubility values measured in the presence of an inert crowding agent.[22,23] Other studies have used descriptive parameters derived from precipitation profiles (e.g., midpoint values) as a means of rapidly rank ordering different solutions conditions for pharmaceutical development.[22−24] Middaugh and co-workers used an extrapolation method to determine the apparent thermodynamic activity of saturated protein solutions from protein precipitation data in solutions with different polyethylene glycol (PEG) concentrations.[25] Measures of nonspecific, weak protein−protein interactions (referred to hereafter as PPI) under different solution conditions are commonly used to interpret protein aggregation data under those same conditions. The rationale behind such approaches is that mechanistically protein aggregation must have one or more association steps. Weak PPI are often characterized using experimental measures of protein charge and/or the second osmotic virial coefficient (B_2).[19,26,27] Using statistical mechanics, the second osmotic virial coefficient can be defined as

$$B_2 = -\frac{N_A}{2M^2}\int\{\exp[-W_{22}(r)/k_BT] - 1\}4\pi r^2 dr \quad (1)$$

where M is the molecular weight of the protein, N_A is Avogadro's number, k_B is the Boltzmann constant, T is the absolute temperature, and $W_{22}(r)$ is the protein−protein potential of mean force (averaged over all orientations) as a function of center-to center distance, r.[28−30] If a protein is globular, and if two protein molecules effectively stick together irreversibly upon association, the kinetics of protein aggregation should closely follow the theory of slow coagulation[31]

$$k \approx \frac{2\pi(D_1 + D_2)}{\int_{R_{s1}+R_{s2}}^{\infty}\exp\{W_{12}(r)/k_BT\}\frac{dr}{r^2}} \quad (2)$$

where k is the rate of association, D_1 and D_2 are the diffusion coefficients of the aggregating species (1 and 2), and $R_{s1}$and R_{s2} are the spherical radii of the aggregating species. $W_{12}(r)$ is the interaction potential between species 1 and 2 as a function of center-to-center distance r. In the scenario described above, we can assume that protein aggregation should directly correlate to B_2. There are several prominent examples in the literature, however, where observed protein aggregation results do not necessarily show any apparent direct correlation to such PPI values.[32,33]

In this work, we seek to understand the role of protein−protein interactions and protein solubility on the mechanism(s) and rate(s) of aggregation for a model IgG1 mAb. We propose that multiple aggregation mechanisms are possible and hypothesize that different pathways may dominate depending upon the fraction of structurally perturbed mAb in solution. Therefore, we present several theoretical kinetic models to explain why protein aggregation may appear to correlate with weak PPI, solubility values, and conformational stability in some cases but not in others. To this end, we generated aggregation data from a stability study with the model IgG1 mAb at different incubation temperatures, time points and solution conditions, to induce varying extents of mAb structural perturbation, and apply our models to examine how protein−protein interactions and solubility values (measured in the presence of PEG), hereafter simply to as solubility, affect mAb aggregation at different temperatures. We then seek to quantitatively investigate and deconvolute the inter-relationships of colloidal protein−protein interactions and solubility on aggregate nucleation and growth steps as a function of temperature-induced structural perturbations of a model IgG1 mAb.

Theory—Kinetic Model of Protein Aggregation. This model uses the framework of the Lumry-Eyring nucleated polymerization model developed by Roberts and co-workers, to consider protein aggregation, in bulk solution, as a multistep process that may involve several competing nucleation and growth pathways.[34,35] The formation of an irreversible dimer (nucleation event) can be described by one or more of the following potentially competing pathways:

$$N^* + N^* \overset{K_{a1,(N^*,N^*)}}{\longleftrightarrow} \{N^*\}_2 F \overset{k_{nuc,\{N^*\}_2}}{\longleftrightarrow} A_{2,\{N^*\}_2} \quad (3a)$$

$$N^* + m \overset{K_{a1,(N^*,m)}}{\longleftrightarrow} \{N^*m\} \overset{k_{nuc,\{N^*m\}}}{\longleftrightarrow} A_{2,\{N^*m\}} \quad (3b)$$

$$m + m \overset{K_{a1,(m,m)}}{\longleftrightarrow} \{m\}_2 \overset{k_{nuc,\{m\}_2}}{\longleftrightarrow} A_{2,\{m\}_2} \quad (3c)$$

Where N^* is a conformationally altered monomer, m is a native monomer, and $A_{2,\{\text{encounter complex}\}}$ is an "irreversible" dimer (net thermodynamic irreversibility relative to the current solution environment) that has formed through an encounter complex intermediate. $\{N^*\}_2$, $\{N^*\ m\}$, and $\{m\}_2$ are reversible encounter complexes whose initial structures should depend upon the structure of the associating species. $K_{a1,(N^*,N^*)}$, $K_{a1,(N^*,m)}$, and $K_{a1,(m,m)}$ are the equilibrium association constants for the reversible dimeric encounter complex formation. Please note that encounter complex formation does not have to be at equilibrium, rather that its formation is reversible and can be described by a forward and reverse rate constant. The subscript of the equilibrium association constant in parentheses is used to differentiate between the aggregating monomer species. k_{nuc} is a rate constant describing conformational rearrangement of an encounter complex to an irreversible aggregate (referred to as nucleation in the LENP model). The subscript of k_{nuc} specifies the type of encounter complex undergoing the nucleation event. Figure 1 is a visual scheme depicting the nucleation mechanisms described by eqs 3a−3c.

After the nucleation event, the existing dimer may enter a growth phase where the oligomeric state of the aggregate grows through the addition of a native monomer, conformationally altered monomer, or an aggregate to the existing structure. This association process is thus represented by the following equations:

$$A_j + N^* \overset{K_{aj,(N^*)}}{\longleftrightarrow} \{N^*A_j\} \overset{k_{g,\{N^*A_j\}}}{\longleftrightarrow} A_{j+1} \quad (4a)$$

$$A_j + m \overset{K_{aj,(m)}}{\longleftrightarrow} \{A_jm\} \overset{k_{g,\{A_jm\}}}{\longleftrightarrow} A_{j+1} \quad (4b)$$

$$A_j + A_i \overset{k_{agg(j,i)}}{\longrightarrow} A_{j+i}\cdots \quad (5)$$

DOI: 10.1021/acs.jpcb.6b03878
J. Phys. Chem. B 2016, 120, 7062−7075

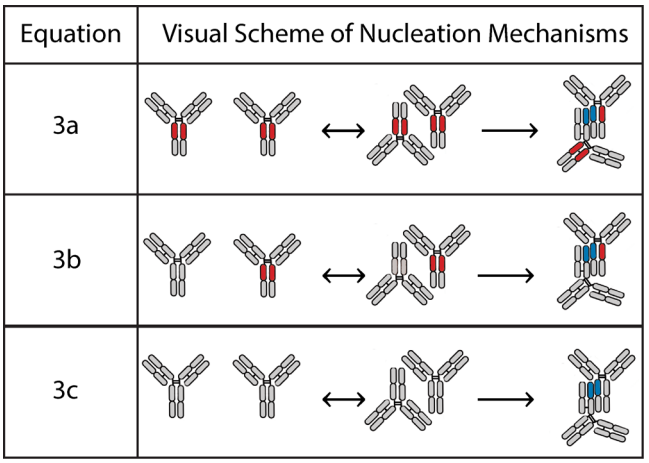

Figure 1. Visual scheme of potential mAb nucleation mechanisms. The various mAb nucleation mechanisms of aggregation shown in the figure correspond to eqs 3a, 3b, and 3c. The visual schematic is not intended to be structurally accurate at a molecular level, and therefore should not be over interpreted in terms of actual mAb aggregate structure. Red color represents a disordered domain, gray color a native domain, and blue color an interdomain structure between two mAbs.

Where j and i represent the number of monomeric units contained within an aggregate, and $2 \leq (\text{j or i}) < \infty$. $K_{\text{aj, }(N^*)}$ and $K_{\text{aj, }(m)}$ represent the equilibrium association constants for growth of an aggregate, composed of j monomers, by addition of a conformationally altered monomer (N^*) or native monomer (m), respectively. Similar to aggregate nucleation, the brackets "{}" denote a reversible encounter complex composed of two species. The rate constant, k_g, describes the conformational rearrangement of an aggregate-monomer encounter complex to a larger, irreversible aggregate. $k_{\text{agg, (j, i)}}$ is a rate constant for the formation of an aggregate composed of j + i monomeric units from two aggregates of size j and i. Figure 2 is a visual scheme depicting the growth mechanisms for different dimers described by eqs 4a, 4b, and 5.

Since we have neglected to specify initial A_j nuclei types in eqs 4a, 4b, and 5, it should be recognized that the equilibrium and rate constants of eqs 4a, 4b, and 5 actually represent apparent values which consider every possible nuclei. To illustrate this point, we consider a simple situation where apparent rate $= k_{\text{app}}[X_{\text{tot}}] = k_1[X_1] + k_2[X_2] + k_3[X_3]$. Thus, $k_{\text{app}} = (k_1[X_1] + k_2[X_2] + k_3[X_3])/[X_{\text{tot}}]$, where $[X_{\text{tot}}] = [X_1] + [X_2] + [X_3]$. To reduce the complexity of the modeling, we proceed with the understanding that equilibrium and rate constants pertaining to aggregate growth represent apparent rate constants which are a convolution of growth rates for every possible nuclei for a given size. If we define the total monomer concentration as being equal to the concentration of native monomer plus the concentration of partially unfolded monomer (i.e., $m_{\text{tot}} = m + N^*$), then eqs 3a–5 can be used to express the rate of monomer loss as

$$-\frac{d[m_{\text{tot}}]}{dt} = 2 \times k_{\text{nuc,obs}}[m_{\text{tot}}]^2 + \sum_{\text{j}=2}^{\infty} k_{\text{g,obs,}\{A_j\}}[A_j][m_{\text{tot}}] \tag{6}$$

where $k_{\text{nuc,obs}}$ and $k_{\text{g,obs}}$ are the observed rate constants for nucleation and growth events and will reflect some

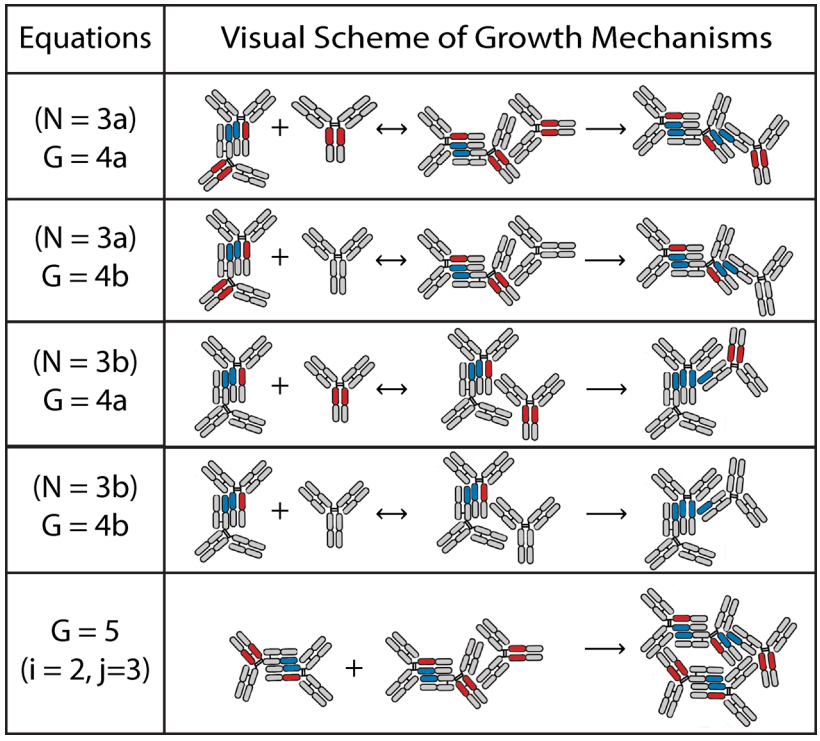

Figure 2. Visual scheme of growth mechanisms for different dimers produced through nucleation mechanism 3a or 3b. The different mAb growth mechanisms of aggregation shown in the figure correspond to eqs 4a, 4b, and 5. The visual schematic is not intended to reflect actual structure at a molecular level, and therefore should not be directly interpreted in terms of aggregate structure. Red color represents a disordered domain, a gray color a native domain, and blue color represents an interdomain structure between two mAbs. The letters G and N represent "growth" and "nucleation," respectively.

DOI: 10.1021/acs.jpcb.6b03878
J. Phys. Chem. B 2016, 120, 7062–7075

combination of the competing aggregation pathways. The first term on the right-hand side of eq 6 describes monomer loss as a result of a nucleation event, and the second term describes monomer loss as a result of monomers adding to aggregates of all possible sizes. The subscript $\{A_j\}$ on $k_{g,obs}$ is used to differentiate between the observed rate constants of growth events for aggregates of different sizes. Additionally, the subscript $\{A_j\}$ on $k_{g,obs}$ intentionally neglects to specify the monomer type (N^* or m) involved in the growth event since the observed rate constant will be a convolution of both growth mechanisms.

The rate of aggregate formation for an aggregate consisting of j monomers can be described by the following equation:

$$\frac{d[A_j]}{dt} = k_{g,obs,\{A_{j-1}\}}[m_{tot}][A_{j-1}] - k_{g,obs,\{A_j\}}[m_{tot}][A_j] - k_{agg(j,j)}[A_j]^2 - [A_j]\sum_{i=2}^{\infty} k_{agg(j,i)}[A_i] + \begin{cases} \sum_{i=2}^{j/2} k_{agg(j-i,i)}[A_{j-i}][A_i] & j \in \text{even integers} \\ \sum_{i=2}^{j-1/2} k_{agg(j-i,i)}[A_{j-i}][A_i] & j \in \text{odd integers} \end{cases} \quad (7)$$

Theory—Role of Conformational Stability on Aggregation Rates. Considering that $k_{nuc,obs}$ is the observed rate constant for three potentially competing pathways, it can be expressed in terms of the observed rate constants for each mechanism and the fraction of conformationally distorted protein, f, where f is assumed to be constant at any given temperature. If we define $N^* = f \times m_{tot}$ and $m = (1 - f) \times m_{tot}$, then

$$k_{nuc,obs} = k_{nuc,obs,\{N^*\}_2} \times f^2 + k_{nuc,obs,\{N^*m\}} \times f(1-f) + k_{nuc,\{m\}_2} \times (1-f)^2 \quad (8)$$

$k_{g,obs}$ for an aggregate of size j can be similarly defined as

$$k_{g,obs,\{A_j\}} = k_{g,obs,\{N^*A_j\}} \times f + k_{g,obs,\{A_jm\}} \times (1-f) \quad (9)$$

If a protein does not aggregate by a particular pathway, then the observed rate constant can simply be set to 0.

Theory—Role of Colloidal Stability and Solubility on Aggregation Rates. The equilibrium constants describing encounter complex formation for aggregate nucleation (i.e., $K_{a1,(N^*,N^*)}$, $K_{a1,(N^*,m)}$, and $K_{a1,(m,m)}$) and aggregate growth (i.e., $K_{aj,(N^*)}$ and $K_{aj,(m)}$) can be described as an association rate constant divided by a dissociation rate constant.

Assuming steady state kinetics can be applied to nucleation ($\frac{d\{N^*\}_2}{dt} = \frac{d\{N^*m\}}{dt} = \frac{d\{m\}_2}{dt} = 0$), the observed rate constant for a particular nucleation mechanism is given by $k_{nuc,obs,\{\}} = \frac{k_{a1,\{\}}k_{nuc,\{\}}}{k_{-a1,\{\}} + k_{nuc,\{\}}}$, where $\{\}$ represents the $\{N^*\}F_2$, $\{N^*m\}$, or $\{m\}_2$ pathway. If the same assumption is applied to aggregate growth, $k_{g,obs,\{\}} = \frac{k_{aj,\{\}}k_{g,\{\}}}{k_{-aj,\{\}} + k_{g,\{\}}}$. When two protein monomer/aggregates species diffuse together to form an encounter complex, there are 2 limiting cases of particular interest: (1) the encounter complex rapidly forms a stable aggregate ($k_{nuc,\{\}} \gg k_{-a,\{\}}$ and/or $k_{g,\{\}} \gg k_{-aj,\{\}}$), and (2) the encounter complex tends to diffuse apart ($k_{-a1,\{\}} \gg k_{nuc,\{\}}$ and/or $k_{-aj,\{\}} \gg k_{g,\{\}}$).

Considering limiting case (1) in further detail, $k_{nuc,obs,\{\}} \approx k_{a1,\{\}}$ and/or $k_{g,obs,\{\}} \approx k_{aj,\{\}}$. Under such conditions, the observed rate constant for a particular mechanism will approximately equal the rate of protein association which is directly related to colloidal stability (see eq 2). This limiting case could occur if the activation energy barrier for encounter complex formation is sufficiently higher than the activation energy barrier for nucleation. When limiting case (2) is further examined, $k_{nuc,obs,\{\}} \approx k_{nuc,\{\}} K_{a1,\{\}}$ and/or $k_{g,obs,\{\}} \approx k_{g,\{\}} K_{aj,\{\}}$. $k_{a1,\{\}}$ and $K_{aj,\{\}}$ are equilibrium constants describing encounter complex formation for a particular nucleation and growth pathway, respectively. $k_{nuc,\{\}}$ and $k_{g,\{\}}$ are rate constants describing conformational rearrangement of the encounter complex into a stable aggregate. Under this limiting case, aggregation kinetics will not be related to colloidal stability in a kinetic sense, but will instead depend upon equilibrium encounter complex formation and subsequent structural rearrangement. If solubility (or extrapolated thermodynamic activity) measurements in solutions with inert crowding agents reflect the thermodynamic favorability of protein in solution vs an amorphous solid phase, it could be used as surrogate parameter to evaluate changes in $K_{a1,\{\}}$ and $K_{aj,\{\}}$ between solution conditions.

MATERIALS AND METHODS

Materials and Sample Preparation. The IgG1 mAb (pI ~ 9) was provided by Janssen Research & Development, LLC (Horsham, Pennsylvania) at an approximate concentration of ~40 mg/mL. Citrate and histidine stock formulation buffers (50 mM) were prepared at pH 4.5 and 6.5 with and without 100 mM NaCl. L-Histidine was obtained from Sigma-Aldrich (St. Louis, Missouri). Citric acid anhydrous and sodium citrate dihydrate were from Fisher Scientific (Hampton, New Hampshire). Buffers were prepared with Milli-Q water (EMD Millipore, Billerica, Massachusetts) and were sterile filtered using a 0.2 μm filter. Final mAb solutions for these studies were prepared at a concentration of 1.0 mg/mL by diluting the mAb stock solution (1/40) into each of the four formulation buffers. The working mAb solutions of 3 mL each were aliquoted into 37.7 × 16.75 mm Fiolax glass vials (Schott, Lebanon, Pennsylvania) capped with elastomeric stoppers that were treated with a fluorocarbon film (West Pharmaceutical Services, Exton, Pennsylvania). The sample preparation procedures outlined above are described as well in a separate but complementary study examining aggregation at the air−water interface in the presence of mechanical agitation.[36] Vials intended for long-term incubation were sealed with flip-off CCS seals (West Pharmaceutical Services). The IgG1 mAb containing sample vials were subjected to shorter term incubation at 57 °C for up to 5 days or longer term incubation for up to 7 months at either 40 or 25 °C.

Differential Scanning Calorimetry (DSC). A VP-Capillary DSC (Malvern Instruments, Worcestershire, United Kingdom) was used to obtain apparent melting thermograms for 1.0 mg/mL mAb in different solution conditions. The differential heat capacity between the mAb solution (sample cell) and corresponding buffer (reference cell) was scanned over a temperature range of 10 to 90 °C at a rate of 1 °C/min. The MicroCal LLC DSC plug-in for Origin 7.0 was used for data analysis by iteratively fitting processed thermograms to a non-two state model for protein unfolding.

DOI: 10.1021/acs.jpcb.6b03878
J. Phys. Chem. B 2016, 120, 7062−7075

Size Exclusion Chromatography (SEC). SEC was performed using a prominence UFLC HPLC system (Shimadzu, Kyoto, Japan) equipped with a diode array detector. A TSKgel G3000SWx1 stainless steel column (Tosoh Biosciences, San Francisco, California) with a TSKgel SWxI guard column were used at 30 °C to separate and quantitate monomer, aggregate, and fragment populations. A pH 6.8, 0.2 M sodium phosphate buffer was used as the mobile phase to reduce protein adsorption to the column.[37] The flow rate was set to 0.7 mL/min and the column was allowed to equilibrate for 3 h prior to measurement. For each sample, 30 μL was injected onto the column and the absorbance at 214 nm was collected for 30 min. LC Solution software from Shimadzu was used to integrate monomer, aggregate, and fragment peaks. Integrated peak areas were normalized by the total area at $t = 0$ to monitor the loss in peak area between different time points.

Sedimentation Velocity Analytical Ultracentrifugation (SV-AUC). An Optima XL-I analytical ultracentrifuge (Beckman Coulter, Fullerton, CA) equipped with an interference optical system was used for sedimentation velocity measurements. Experiments were conducted at 20 °C, at a rotor speed of 40 000 rpm. Samples and reference were loaded into Beckman charcoal-Epon two sector cells with 12 mm sapphire windows. The samples were incubated within the centrifuge for an additional hour after the chamber reached temperature. Analysis of the sedimentation data was performed using Sedfit software.[38] A continuous sedimentation coefficient distribution c(s) was used with 100 scans of the sedimentation data to determine monomer and aggregate content in pH 4.5, 50 mM histidine mAb samples incubated at 57 °C. The partial specific volume, buffer density and viscosity values used to model the data were 0.73 mL/g, 1.00 g/mL, and 1.002 cP, respectively. A range of 0 to 30 s was used (after verifying that there was no signal outside of this range) with a resolution of 300 points per distribution and a confidence level of 0.95. Baseline, radial independent noise, and time independent noise were fit by the software. The meniscus and bottom positions were set manually. Integrated peak areas were normalized by the total area at $t = 0$ to monitor the loss in peak area between different time points.

Static Light Scattering. Composition gradient multiangle light scattering (CG-MALS) was performed to determine the apparent second virial coefficient (A_2) of the various mAb solutions. The CG-MALS configuration consisted of a Calypso-II equipped with 20 nm polyether sulfone (PES) membrane filters to mix, degas, filter and inject mAb concentration gradients into a Dawn Heleos II multiangle light scattering (MALS) detector with a 658 nm laser for static light scattering (Wyatt Technology Corp, Santa Barbara, CA), and an in-line Optilab rEX differential refractive index detector to measure protein concentration. Protein solutions for light scattering were purified by performing four 15× dilution buffer exchanges using Amicon Ultra-15 10 kDa molecular weight cutoff centrifugal filter devices (EMD Millipore, Billerica, MA). After the final buffer exchange, the protein and the buffer fractions were collected and filtered using a Whatman 0.1 μm PVDF syringe driven membrane filter (GE Healthcare, Little Chalfont, United Kingdom) to remove large impurities. Protein concentrations were measured with a NanoDrop spectrophotometer (Thermo Fisher Scientific, Waltham, MA) using a 0.1% extinction coefficient of 1.4 at 280 nm. The initial target protein concentration for static light scattering experiments was ∼10 mg/mL. If $|2A_2M_wc_2| \leq 0.05$ then the protein concentration was increased to ∼30 mg/mL for subsequent experiments, where $|2A_2M_wc_2|$ is a unit-less fraction that reflects the contribution of nonideal interactions to the total light scattering signal. A_2 is the apparent second virial coefficient, M_w is the weight-averaged molecular weight, and c_2 is the protein concentration. The apparent second virial coefficient was determined by regressing SLS data at multiple protein concentrations using the Zimm equation[39]

$$\frac{K^*c_2}{R(\theta)} = \frac{1}{M_w} + 2A_2c_2 \tag{10}$$

where $R(\theta)$, the excess Rayleigh ratio, describes the intensity of scattered light. K^* is an optical constant given by

$$K^* = \frac{4\pi^2 n_0^2}{N_A\lambda_0^4}\left(\frac{dn}{dc}\right)^2 \tag{11}$$

where n_0 is the refractive index of the buffer, λ_0 is the wavelength of the laser in a vacuum, N_A is Avogadro's number, and $\frac{dn}{dc}$ is the differential refractive index increment of the protein. The value of $\frac{dn}{dc}$ was set to 0.185 mL/g.

Using statistical mechanical arguments, the theoretical contributions of excluded volume to the second osmotic virial coefficient can be expressed as[31]

$$B_2 = \frac{N_A u}{2M^2} \tag{12}$$

where is M the molecular weight of the protein, and u is the excluded volume. The excluded volume for a spherical system can be expressed as $8V$, where V is the volume of a single sphere. Therefore, the theoretical contribution of excluded volume on the apparent second virial coefficient can be calculated for spherical particles[40] by

$$B_2^{\text{exc}} = \frac{16\pi N_A r^3}{3M^2} \tag{13}$$

Experimental apparent second virial coefficients were then normalized by B_2^{exc} to provide a unitless parameter sensitive to protein−protein interactions:

$$a_2 = \frac{A_2 - B_2^{\text{exc}}}{B_2^{\text{exc}}} \tag{14}$$

Using M = 150 000 Da and a spherical diameter of 10 nm, $B_2^{\text{exc}} = 0.556 \times 10^{-4}$ mol ml g^{-2}. The normalized virial coefficient calculations described above are built into the Calypso V2.1.3 software. The reported normalized a_2 values in this manuscript are an average of three separate experiments.

Polyethylene Glycol (PEG) Precipitation. Stock solutions of PEG-10,000 ranging from 0 to 40% w/v were prepared for each buffer condition. Each solution (244 μL, 0 to 40% w/v) was added to a 96-well polystyrene filter plate (Corning Life Sciences, Corning, NY). Six microliters of an IgG1 mAb stock solution (∼40 mg/mL) was added to the wells to achieve final protein concentrations of 1 mg/mL. The plates were incubated overnight at room temperature and centrifuged at 3500g for 15 min. The filtrate was collected in a clear 96 well collection plate (Greiner Bio-One North America Inc., Monroe, NC). Afterward, 200 μL of the filtrate was transferred into a 96 well UV Star microplate. The filtrate was measured using SpectraMax M5 UV−visible plate reader (Molecular Devices LLC, Sunnyvale, CA) at 280 nm to determine the protein

DOI: 10.1021/acs.jpcb.6b03878
J. Phys. Chem. B 2016, 120, 7062−7075

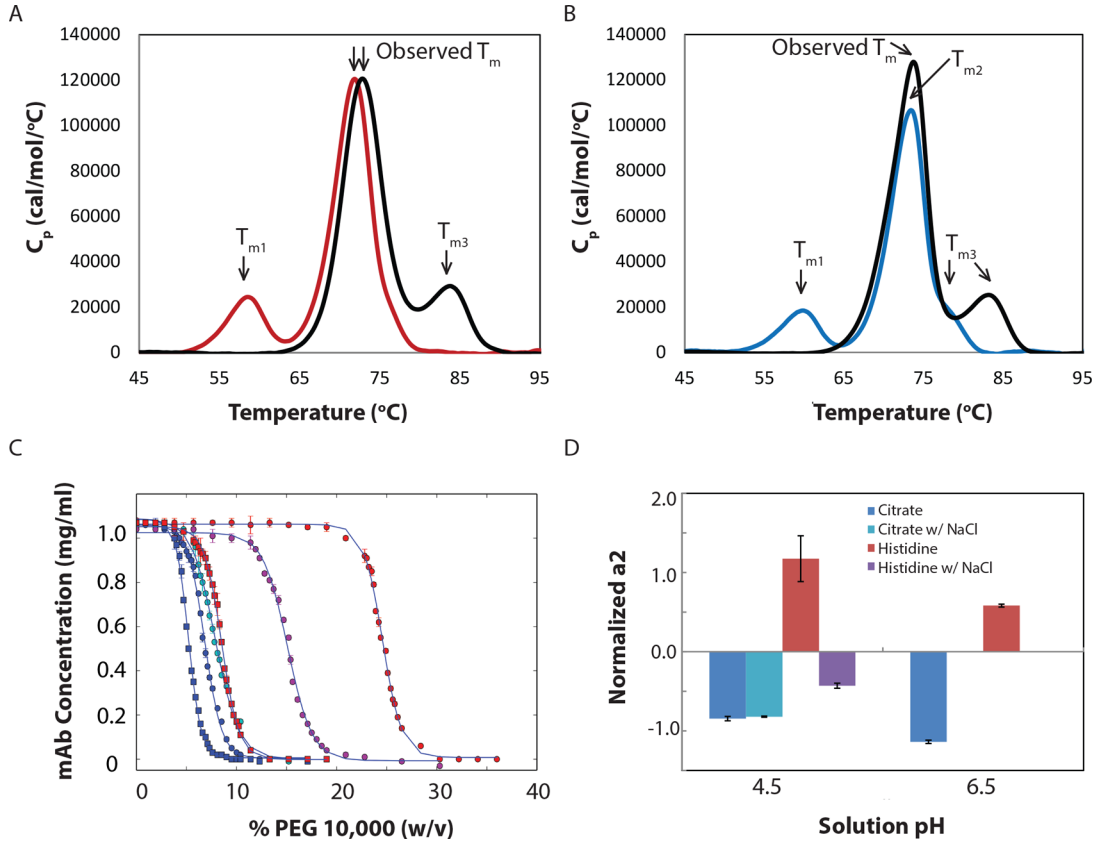

Figure 3. Representative conformational stability, solubility with PEG, and protein−protein interactions data for IgG1 mAb in different pH and buffer conditions. (A) DSC thermogram of mAb in pH 4.5 (red trace) and pH 6.5 (black trace) histidine buffer. (B) DSC thermogram of mAb in pH 4.5 (blue trace) and pH 6.5 (black trace) citrate buffer. A thermal melting profile that fails to display a melting temperature for each domain is labeled with an observed T_m to highlight that the melting event could be a convolution of two domain unfolding events. (C) Protein-PEG precipitation curves for 1 mg/mL mAb at pH 4.5 (denoted by circles) and pH 6.5 (squares) in histidine buffer (red), histidine buffer w/100 mM NaCl (purple), citrate buffer (blue), and citrate buffer w/100 mM NaCl (cyan). (D) Normalized second virial coefficient values at pH 4.5 and 6.5 in citrate buffer (blue), citrate buffer w/100 mM NaCl (cyan), histidine buffer (red), and histidine buffer w/100 mM NaCl (purple) as measured by static light scattering (CG-MALS).

concentration. Concentration of IgG1 mAb vs % PEG-10,000 data were fit using a standard four-parameter modified Hill-slope sigmoidal curve equation:

$$y = b + \left(\frac{t - b}{1 + e^{s(\mathrm{mid} - x)}}\right) \quad (15)$$

where t = top plateau, b = bottom plateau, mid = x-axis midpoint, and s = slope. Midpoint values were determined from the resulting curve fit as described in detail elsewhere.[24]

Determination of Aggregation Kinetic Rate Constants. Rate constants describing the aggregation process ($k_{nuc,obs}$ and $k_{g,obs}$) were determined by simulating fits to experimental SEC data using an in-house script in Python v2.7.10. The script iteratively solves eqs 6 and 7 based on user entered values for the number of time steps; range of aggregate polymerization (j); and rate constants $k_{nuc,obs}$, $k_{g,obs}$, and k_{agg}. Simulated monomer loss as a function of time was compared to experimental monomer loss presumably due to aggregation (and with fragment peaks treated as monomer). SV-AUC was used to measure monomer loss (instead of SEC) for stressed mAb samples in certain formulations that were determined to adsorb to the SEC column (see text). Aggregate−aggregate association was set to zero in mathematical simulations, and $k_{g,obs}$ was treated as constant for all aggregate sizes ($k_{g,obs,\{A_2\}} \approx k_{g,obs,\{A_\infty\}}$). Additionally, the polymerization state j was set to ∞ to reduce the amount of data points required to distinguish between simulations. The effects and purpose of these modeling parameters and treatments are discussed in the Supporting Information. Simulations were performed for each sample until the residuals (experimental data point−simulated data point) were within the range of the experimental standard deviation and randomly distributed about zero.

Empirical Modeling of Net Protein Charge. The molecular modeling and visualization program PyMol v1.5 was used to construct the Fab, hinge, and Fc regions of an IgG1 antibody model.[41] The Fab and hinge coordinates were obtained from the *in silico* KOL-Padlan structure of an IgG1 molecule.[42] Homology models of the antibody sequence were mapped onto the template Fab regions with Modeler version 9.12.[43] The Fc region was retrieved from the X-ray structure, 3AVE, maintaining the linked G0F glycan residues.[44]

The homology model was analyzed using PROPKA v3.1, an empirical algorithm that calculates the pK_a of titratable residues based on interactions with nearby functional groups and desolvation effects due to the structural position of the residue.[45,46] The net charge of the IgG1 mAb was then calculated using the Henderson−Hasselbalch relationship with user entered pH values and titratable residue pK_a values from the PROPKA 3.1 results.

DOI: 10.1021/acs.jpcb.6b03878
J. Phys. Chem. B 2016, 120, 7062−7075

RESULTS AND DISCUSSION

Conformational Stability of mAb under Different Solution Conditions. As a first step to better understand the relationship between temperature and observed aggregation rates, differential scanning calorimetry (DSC) was used to assess how changes in solution conditions (pH, ionic strength, buffer ion type) affect the thermal onset (T_0) and thermal melting temperature values (T_m) for an IgG1 mAb. It has previously been shown that IgG1 mAbs undergo thermal unfolding steps which correspond to structural alterations of distinct domains/regions of the antibody.[47,48] We apply the model proposed by Ionescu and co-workers to interpret deconvoluted thermal melting events for this IgG1 mAb in terms of its CH_2 domain, Fab region, and CH_3 domain unfolding events as previously shown for three other IgG1 mAbs.[49]

The IgG1 mAb used in this study displays two endothermic transitions at pH 4.5 and 6.5 in histidine buffered solutions as measured by DSC (Figure 3A). At pH 4.5, the first melting transition can be attributed to unfolding of the CH_2 domain and the second larger transition is probably a convolution of Fab region and CH_3 domain unfolding events.[49] The first melting temperature (T_{m1}) was at 58.3 ± 0.1 °C, and the second was at 71.7 ± 0.1 °C. Addition of 100 mM NaCl to the pH 4.5 histidine solution did not change the number or order of the observed transitions in the DSC thermogram, but the T_{m1} value for the mAb decreased to 56.1 ± 0.1 °C and the second T_m decreased to 70.3 ± 0.1 °C (Table 1). The decrease in T_m values, compared to the NaCl absent solution, signifies a decrease in the conformational stability of this mAb, but it could also be an artifact caused by faster aggregation rate constants.[50] At pH 6.5, the mAb in the histidine solution also displayed two endothermic transitions (Figure 3A). In this case, however, the first transition is probably a convolution of CH_2 domain and Fab region unfolding[49] with an observed T_m value at 72.9 ± 0.1 °C while the second transition reflects unfolding of the CH_3 domain with a T_{m3} at 79.2 ± 0.1 °C. A summary of the apparent thermal onset and thermal melting temperatures for the mAb, in each of the histidine solutions, are summarized in Table 1.

Table 1. Apparent Thermal Melting Temperatures for mAb in Solution Conditions As Measured by DSC[a]

solution condition (1 mg/mL mAb)	T_{onset} (°C)	T_{m1} (°C)	T_{m2} (°C)	T_{m3} (°C)
pH 4.5 histidine	50.1	58.3	71.7	
pH 4.5 histidine w/100 mM NaCl	47.8	56.1	70.3	
pH 6.5 histidine	62.8	72.9		83.4
pH 4.5 citrate	51.5	59.5	73.1	79.2
pH 4.5 citrate w/100 mM NaCl	50.1	59.0	72.7	79.0
pH 6.5 citrate	62.0	73.1		83.1

[a]Apparent thermal melting temperature values are reported as T_{m1}, T_{m2}, and T_{m3} representing the CH_2, Fab, and CH_3 domains of the mAb, respectively (see Figure 1 and text). A thermal melting profile that fails to display melting temperatures for each domain/region is considered an observed T_m to highlight that the melting event could be a convolution of two unfolding events. Each reported value is the average of $n = 3$ experiments, and the standard deviation (SD) for each value was less than 0.2 for all conditions.

DSC thermograms of the mAb in pH 4.5 and 6.5 citrate solutions had higher onset and melting temperatures compared to the mAb in histidine solution (Figure 3B). At pH 4.5, there were 3 endothermic transitions with the first, second, and third corresponding to the CH_2 domain, Fab region, and CH_3 domain, respectively.[49] Melting temperatures for the first, second and third transitions were 59.5 ± 0.1, 73.1 ± 0.1, and 79.2 ± 0.1 °C, respectively. Addition of 100 mM NaCl, to the pH 4.5 citrate formulation decreased the melting temperatures slightly with T_{m1}, T_{m2}, and T_{m3} values decreasing to 59.0 ± 0.1, 72.7 ± 0.1, and 79.0 ± 0.1 °C, respectively (Table 1). Interestingly, the mAb melting temperatures decreased more when NaCl was added to the histidine solution than when it was present in the citrate solution. This could be because the ionic strength of the histidine solution was substantially lower than the citrate solution (see calculated ionic strength values for each condition summarized in Table 2). At pH 6.5, the mAb in citrate solution displayed 2 endothermic transitions similar to the pH 6.5 mAb histidine solution. The first transition is presumably a convolution of CH_2 domain and Fab region unfolding with an observed T_m occurring at 73.1 ± 0.1 °C and the second transition reflecting unfolding of the CH_3 domain with a T_{m3} at 83.1 ± 0.1 °C.

Table 2. Summary of Experimental and Calculated Physical Parameters of Different mAb Solutions[a]

				experimental a_2		[PEG] midpoint
solution conditions (1 mg/mL mAb)	pH	approx. mAb net charge	approx. ionic strength	mean	SD	mean
50 mM citrate	4.5	104.3	0.089	−0.84	0.03	6.8
50 mM citrate	6.5	41.3	0.243	−1.14	0.02	5.2
50 mM citrate w/ 100 mM NaCl	4.5	104.3	0.189	−0.82	0.01	7.9
50 mM histidine	4.5	104.3	0.024	1.18	0.29	24.6
50 mM histidine	6.5	41.3	0.007	0.58	0.02	8.5
50 mM histidine w/100 mM NaCl	4.5	104.3	0.124	−0.43	0.03	15.1

[a]Values for approximate mAb net charge, approximate solution ionic strength, and Theoretical b_2 values (theoretical surrogate parameter for protein−protein interactions) were calculated as described in the Materials and Methods section. The experimental surrogate parameter for protein−protein interactions (a_2) and [PEG] midpoint values (midpoint of mAb vs PEG concentration curves; see text) are presented as the average and standard deviation of 3 experiments. Values of b_2 and a_2 are normalized and therefore have no units. [PEG] midpoint has units of % w/v. The standard deviation for the [PEG] midpoint was less than 0.1 for all conditions.

Solubility of mAb under Different Solution Conditions. Protein solubility as a function of polyethylene glycol (PEG) concentration was measured to better understand the thermodynamics of mAb precipitation in different solution environments. The solubility values were extrapolated to determine the apparent thermodynamic activity of saturated mAb solutions without PEG.[25] Representative experimental data showing mAb concentration in different solutions as a function of PEG concentration are presented in Figure 3C. Extrapolated apparent thermodynamic activity values (in the absence of PEG) and [PEG] midpoint values (i.e., 50% of the mAb in the amorphous phase) were determined. In pH 4.5 histidine solution, the mAb had the highest [PEG] midpoint value of 24.6% w/v (with an extrapolated activity value of 1.86 ± 0.4 g/mL). Addition of 100 mM NaCl to the pH 4.5

DOI: 10.1021/acs.jpcb.6b03878
J. Phys. Chem. B 2016, 120, 7062−7075

histidine formulation caused the precipitation curve to shift to a midpoint value of 15.1% w/v PEG (with an extrapolated activity value of 1.10 ± 0.08 g/mL) corresponding to an increase in the ionic strength of the solution. At pH 6.5, the midpoint value was 8.5% w/v PEG (with an extrapolated activity value of 0.11 ± 0.01 g/mL). The mAb in the citrate solutions had [PEG] midpoint values ranking as follows and the values are summarized in Table 2: pH 4.5 citrate + NaCl > pH 4.5 citrate > pH 6.5 citrate. The activity values for the mAb were 0.04, 0.01, and 0.02 g/mL for the pH 4.5, pH 4.5 + NaCl, and pH 6.5 citrate solutions, respectively.

Mahadevan and Hall developed a statistical mechanical model to predict trends in protein solubility/PEG solutions by considering excluded volume, osmotic and electrostatic interactions.[51] In general, our observed results are consistent with their model because solubility values in mAb solutions with PEG decreased with decreasing calculated values of protein charge and/or increased solution ionic strength (see calculated charge and ionic strength values for each condition summarized in Table 2). As described previously in other studies,[22,23] and as described in our experiments below, these descriptive parameters derived from the PEG precipitation profile can be valuable for interpreting observed protein aggregation data under different solution conditions.

The PEG concentration (% w/v) vs protein concentration (i.e., precipitation) profile of this mAb was fit to a sigmoidal function and the [PEG] midpoint values (Figure 3C) were used to compare the relative thermodynamic favorability of non-specific IgG1 mAb associations leading to amorphous precipitation. We hypothesize that differences in the solubility values of the mAb in different solutions could indicate differences in the thermodynamic favorability of transient encounter complex formation. At the [PEG] midpoint, $K_{eq} = \frac{[mAb]_{precipitate}}{[mAb]_{solution}} = 1$. The Gibbs free energy difference ($\Delta G = G_{solution} - G_{precipitate}$) between a protein molecule in solution and solid amorphous phase is zero at the [PEG] midpoint because $\Delta G = RT \ln K_{eq}$. If $G_{precipitate}$ remains unchanged, then an increase in the [PEG] midpoint reflects a decrease in $G_{solution}$ because more PEG is required to increase $[mAB]_{precipitate}$ to achieve $K_{eq} = 1$.

Additionally, the protein−protein potential of mean force (PMF), $W_{22}(r)$, can be expressed as[27,30]

$$W_{22}(r) = W_{HS}(r) + W_Z(r) + W_{disp}(r) + W_{osmotic}(r) + W_{dipole}(r) + W_{assoc}(r) \quad (18)$$

From left to right, the terms on the right-hand side of eq 18 represent contributions of excluded volume, electrical double layer, dispersion forces, osmotic forces, dipole interactions, and specific interaction sites to the protein−protein PMF.[27,30] As the concentration of PEG is increased, the short-range osmotic potential reflected by the $W_{osmotic}(r)$ term becomes increasingly attractive. These osmotic attractions have been previously modeled using a theory developed by Asakura and Oosawa.[52,53] Based on these models, differences in [PEG] midpoint values should approximately reflect the extent to which osmotic forces are required to overcome other repulsive interactions and induce mAb precipitation. On the other hand, this approach has some limitations. For example, Sarangapani et al. have demonstrated that such models can be inadequate for describing protein behavior with changes in pH or protein concentration because they neglect to account for changes in intrinsic flexibility and conformation.[54] Additionally, this approach assumes that the PEG molecules are inert and do not interact with the protein molecules which may not always be the case.

Colloidal Stability of Native mAb under Different Solution Conditions. To compare protein−protein interactions (PPI) in different solution conditions on a relative basis, static light scattering was used to obtain normalized apparent second virial coefficient (a_2) values for the IgG1 mAb as a function of solution pH, ionic strength, and buffer ion type (Figure 3D). Traditionally, the second virial coefficient A_2, obtained from classical analysis of static light scattering data (eq 10), was equated to the second osmotic virial coefficient, B_2.[31,55] More recently, however, the two virial coefficients have been shown to formally differ.[29,56,57] Under sufficiently dilute conditions (e.g., $|2A_2M_wc_2| \leq 0.12$), differences between A_2 and B_2 are not significant in terms of statistical uncertainty.[57−59] Otherwise, the value of A_2 was theoretically proposed to systematically overestimate repulsive interactions and underestimate attractive interactions compared to B_2.[57] In protein solutions with weak PPI, the second virial coefficient can be dominated by contributions from excluded volume.[60] Normalization of the second virial coefficient by correcting for the excluded volume contribution of spheres ($A_2 \rightarrow a_2$) is used to help tease out weak protein−protein interactions.[61,62]

In solutions containing histidine, the IgG1 mAb was found to have the most repulsive PPI with a_2 values of 1.18 ± 0.29 and 0.58 ± 0.02 at pH 4.5 and 6.5, respectively (Figure 3C and Table 2). The mAb in these histidine solutions were the only conditions where $|2A_2M_wc_2| > 0.12$. Addition of 100 mM NaCl to the pH 4.5 histidine solution changed the sign of a_2 from positive to negative, to a value of −0.43 ± 0.03, suggesting that PPI changed from repulsive to slightly attractive for the mAb (Figure 3C). In the pH 4.5 and 6.5 citrate containing solutions, the mAb had the lowest values of a_2 which argues that the mAb under these conditions had the most attractive PPI. This result was notable because the pH 4.5 histidine solution with NaCl has a greater calculated ionic strength than the pH 4.5 citrate solution (Table 2). Addition of 100 mM NaCl to the pH 4.5 citrate formulation did not significantly change the a_2 value despite substantially increasing the ionic strength of the solution. At pH 6.5, the mAb in the citrate solution had the most attractive PPI. This result was expected because the solution had the highest ionic strength and the mAb had the lowest calculated net charge of all conditions tested (see Table 2 for summary of the calculated protein charge and solution ionic effect values).

Experimental and Modeled mAb Aggregation Results in Different Solutions. Using experimental data from either SEC or SV-AUC, monomer loss as a function of time can be used to obtain an apparent reaction order and time scale for protein aggregation. If the size of aggregates remains small, dimers are the smallest aggregate species, and aggregate−aggregate association can be neglected. Then, completely nucleation dominated aggregation should have an effective reaction order of 2. In contrast, aggregation dominated by monomer addition growth mechanisms will have an effective reaction order that approaches 1 if reversible self-association is negligible as is the case for this mAb (data not shown). Under this particular limiting case, monomer loss of this mAb can be modeled and used to obtain rate constants and/or characteristic time scales for both aggregate nucleation and growth by monomer addition.[35]

DOI: 10.1021/acs.jpcb.6b03878
J. Phys. Chem. B 2016, 120, 7062−7075

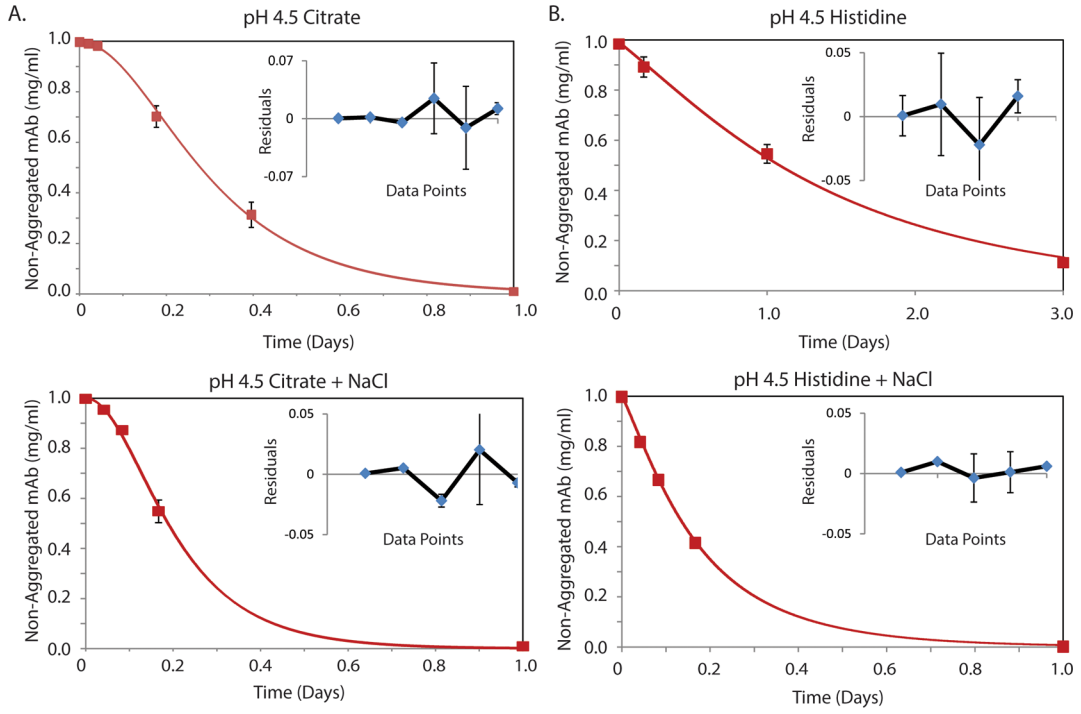

Figure 4. Simulated fit of experimental SEC and SV-AUC data of loss of nonaggregated (monomer + fragment) mAb over time at 57 °C. Experimental (solid red squares, $n = 3$) and simulated profiles (solid red line) of nonaggregated mAb concentration in presented in the upper right corner of the corresponding graph. Error bars reflect the experimental standard deviation. Buffer conditions are labeled above each graph. The top panel of (B) was acquired using SV-AUC and all other conditions were measured using SEC.

Prior to modeling the kinetics of experimental mAb aggregation data sets, simulations of eqs 6 and 7 were performed to better understand how nucleation and aggregate growth affect the overall observed rate of the aggregation process. The effect of varying nucleation and growth rate constants on the simulation was investigated systematically over 4 orders of magnitude for nucleation and 3 orders of magnitude for growth (see Supporting Figure S1). Although it was possible to simulate several conditions that resulted in a similar amount of aggregation over a certain time period, the profiles clearly displayed characteristic differences thereby supporting our modeling approach of fitting monomer loss vs time for this mAb. For example, samples with slower nucleation rates and faster growth rates displayed an initial "lag" phase compared to samples with a faster nucleation rate and slower growth rate. Based on the results of these initial simulations, we collected a range of experimental mAb aggregation stability data in different solutions to capture the perceived lag caused by slower nucleation rates and acceleration produced by fast growth rates. The time scale of the stability study for each mAb solution condition needed to be optimized to capture a full range of aggregation data to properly discriminate between different combinations of nucleation and growth rates.

Simulated fits of experimental mAb aggregation data were then generated for the fraction of nonaggregated mAb species (monomer + fragment) for each solution and temperature condition to determine observed rate constants for aggregate nucleation and growth processes. The rationalization for modeling both monomer and fragments populations as aggregate prone species is discussed in detail the Supporting Information (see Rationalization of Assumptions Present in Aggregation Model). Briefly, substantial fragmentation did not appear to deplete reactive species populations by causing mAb aggregation rates to decelerate. In this work, it should be understood that apparent nucleation and growth rate constants could represent a convolution of pathways where the reactive species could either be a monomer or a fragment for conditions where fragmentation is significant (e.g., incubation at 40 °C). For illustrative purposes, let us consider a hypothetical example where only dimers occur. In this case, eq 6 reduces to

$$-\frac{d[m_{tot}]}{dt} = 2 \times k_{nuc,obs}[m_{tot}]^2$$
$$= 2(k_{nuc,fr^2}[fr]^2 + k_{nuc,fr\times m}[fr][m] + k_{nuc,m^2}[m]^2)$$

where fr represents fragments, m represents monomeric species, and $m_{tot} = m + fr$ in this example. The observed rate constant still provides a good description of the total nucleation without making any further assumptions about the contributions of fragmentation to aggregation rates. In a future study, we plan to investigate the effect of considering fragmentation as the initiation step in separate mAb aggregation pathways to more accurately model such cases.

Representative SEC chromatograms and SV-AUC data demonstrating separation profiles and peak integration of the different mAb species are presented in Supporting Figure S2 (panels A,B). In addition, integrated SEC aggregation profiles for mAb samples under different histidine buffer solution conditions as a function of time and temperature are presented in Supporting Figure S2 (panels C−H). Integrated SEC aggregation profiles for the mAb in different citrate buffer solution conditions at different temperatures are shown in Supporting Figure S3.

Figure 4 shows the simulation results for the SEC aggregation data for the pH 4.5 mAb solutions, in both citrate

DOI: 10.1021/acs.jpcb.6b03878
J. Phys. Chem. B 2016, 120, 7062−7075

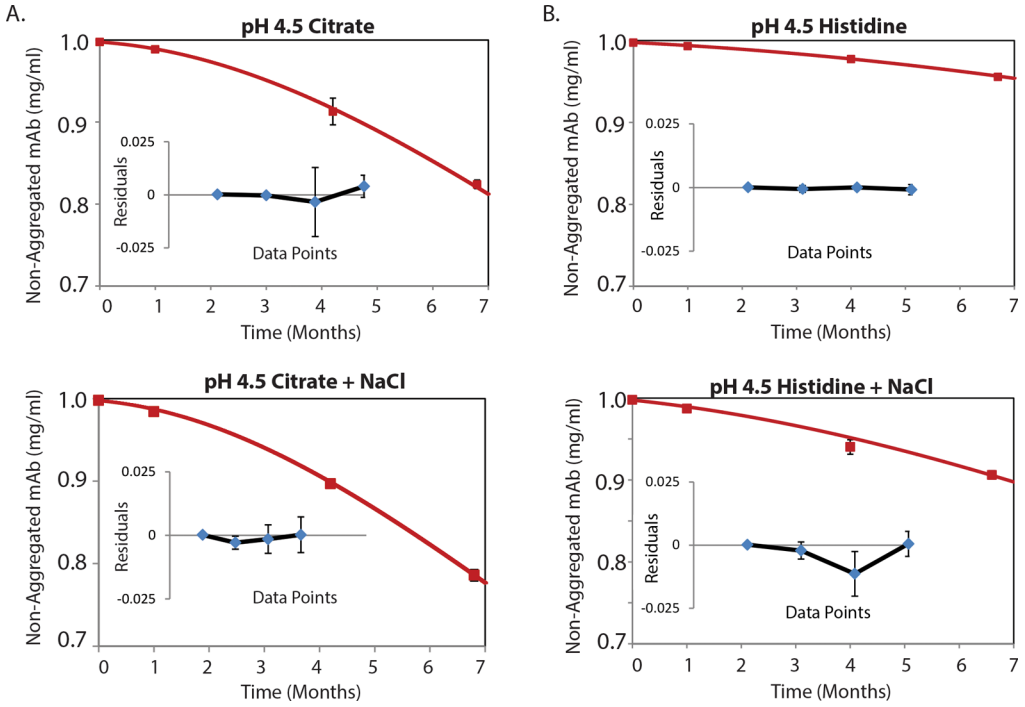

Figure 5. Simulated fit of experimental SEC data of loss of nonaggregated (monomer + fragment) mAb over time at 40 °C. Experimental (solid red squares, n = 3) and simulated profiles (solid red line) of nonaggregated mAb concentration in different solution conditions as a function of incubation time as measured by SEC. The residuals of each fit are presented in the lower left corner of the corresponding graph. Error bars reflect the experimental standard deviation. Buffer conditions are labeled above each graph.

and histidine buffers with/without NaCl, after being incubated at 57 °C for up to 5 days. The red squares in the figure represent the average concentration (mg/mL) of nonaggregated species for mAb solutions in three different sample vials measured by SEC or SV-AUC. In the pH 4.5 citrate solution, incubation resulted in rapid monomer loss with no monomer detected in solution after 1 day of incubation (Figure 4A, top panel). Absorbance spectroscopy of the supernatant fraction after centrifugation confirmed that loss of monomer was because of non-native amorphous precipitation (Supporting Figure S4, panel A). Additionally, the modeled observed growth rate constant dominated the overall aggregation kinetics compared to the nucleation process as determined by the modeled fit. The mAb in the pH 4.5 citrate solution with NaCl also had a similar rate of monomer loss (Figure 4A, bottom panel) and also underwent phase separation after 1 day. The overall kinetics of aggregation was also growth dominated as determined by the modeled fit. On the other hand, although monomer loss of the mAb in the pH 4.5 histidine solution was also rapid (Figure 4B, top panel), no significant increase (compared to t = 0) in the calculated mass of larger aggregates (i.e., particles larger than 2 μm in diameter), based on FlowCam particle data, was detected after 3 days (Supporting Figure S4, panel B). The shape of the simulated result also suggests that the mAb sample has a nucleation dominated aggregation mechanism similar to the light blue trace in Supporting Figure S1, panel A. Increasing the ionic strength of the mAb in histidine buffer (with NaCl) causes the observed aggregation rate to increase, and resulted in significant non-native phase separation after 1 day of incubation (Supporting Figure S4, panel A). In this sample condition, neither aggregate nucleation nor growth clearly dominated the aggregation mechanism (Supporting Table S1). If modeled individually, the experimental variability resulted in relative standard deviation of 10% for aggregate nucleation and 23% for aggregate growth rate constants for the mAb in a pH 4.5 citrate solution incubated at 57 °C. Other experiments performed at this temperature condition had less uncertainty arising from experimental variability.

The pH 4.5 mAb solutions, in both citrate and histidine buffers with/without NaCl, were also incubated at 40 °C for up to 7 months (Figure 5). Integrated SEC results for mAb samples incubated at 40 °C as a function of time are presented in Supporting Figure S3. Less mAb aggregated over the course of 7 months when incubated at 40 °C compared to 1 day at 57 °C. The mAb in the pH 4.5 citrate solutions with and without NaCl had similar rates of aggregation at 40 °C (Figure 5A). In these sample conditions, a slower "lag phase" in which aggregate nucleation primarily occurs was observed prior the rate accelerating due to aggregate growth. The simulated rate constant values support these observations because the observed rate constants of aggregate growth were ∼3 orders of magnitude larger than those of nucleation (Supporting Table S1). On the other hand, a lag phase was not readily observable in the pH 4.5 histidine mAb solutions with and without NaCl (Figure 5B), but the profile displayed some early curvature indicative of both aggregate nucleation and growth processes occurring. The simulated rate constants, however, suggest that the observed growth rate constant was ∼3 orders of magnitude larger than the nucleation rate constant. Although aggregate growth was nontrivial, no significant increases in the calculated mass of larger aggregates (i.e., particles greater than 2 μm in diameter), as calculated from the experimentally determined MFI data, was detected after 7 months (Supporting Figure S4, panel C). If modeled individually, the experimental variability resulted in relative standard deviations of less than 10% for aggregate nucleation and aggregate growth rate constants for all of the conditions at 40 °C. A larger concern in terms of error is

DOI: 10.1021/acs.jpcb.6b03878
J. Phys. Chem. B 2016, 120, 7062−7075

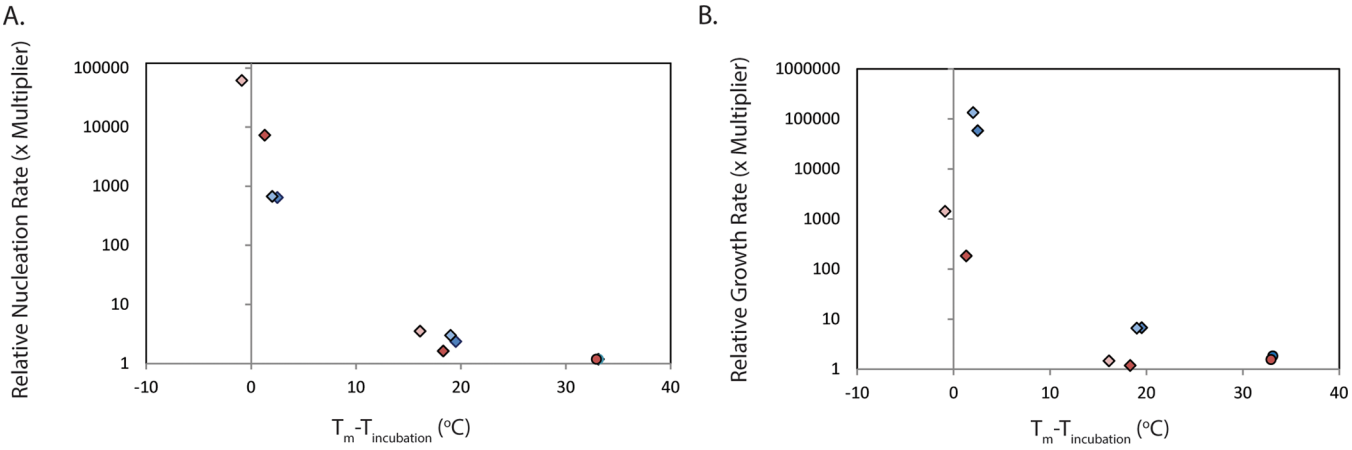

Figure 6. The effect of conformational stability (presence of partially unfolded mAb species) on the observed rate constants for mAb aggregate nucleation and growth. Observed nucleation and growth aggregation rate constants were obtained by fitting simulations of eqs 6 and 7 to experimental SEC and SV-AUC stability data for mAb stored in different solutions at different temperatures. The values reported are dimensionless numbers which were normalized by the smallest observed rate constant for each process. The colors dark blue, light blue, dark red, and light red correspond to the mAb prepared in the citrate, citrate + NaCl, histidine, and histidine + NaCl solution conditions where the diamond and circle shapes correspond to solution pH values of 4.5 and 6.5, respectively. (A.) Modeled values for the observed nucleation rate constant as a function of the first apparent melting temperature (measured by DSC) minus incubation temperature. (B.) Modeled values for the observed growth rate constant as a function of first apparent melting temperature (measured by DSC) minus incubation temperature.

the possibility of degenerate solutions due to the limited range of mAb aggregation data collected at this temperature condition. For example, equally good fits could be obtained by increasing the rate constant for nucleation and decreasing the value for aggregate growth. Fortunately, degenerate solutions could be ruled out for conditions where aggregate−aggregate association was negligible (as was the case at this temperature) by comparing the soluble aggregate fractions measured by SEC to the modeled results. The uncertainty in the modeled values was ~ ± 20% for the mAb sample at pH 4.5 histidine buffer (the solution condition with the smallest range of monomer loss) after comparing modeled results to the soluble aggregate fraction.

The mAb samples at pH 6.5 were also incubated at 40 °C for up to 7 months and fit to the kinetic models described by eqs 6 and 7 (Supporting Figure S5). The rate and extent of aggregation at pH 6.5 were much less than those at pH 4.5, despite reduced values of solubility (and extrapolated thermodynamic activity, determined by PEG precipitation) and having more attractive PPI (A2 values by static light scattering). Curvature of the simulated fit to the experimental SEC aggregation data was also observed for mAb in pH 6.5 citrate solution incubated at 40 °C. The aggregation profile for the mAb in the pH 6.5 histidine solution did not display major curvature since both the modeled nucleation and growth rates were very slow over this time period.

At 25 °C, the aggregation profiles for the mAb in the pH 4.5 histidine and citrate solutions was even slower with less than 3% monomer loss occurring in both samples after 7 months (Supporting Figure S6). Although such degradation could be considered significant from a pharmaceutical storage stability perspective, the modeled nucleation and growth rate constants for both conditions were extremely slow and did not show any appreciable differences between the samples. To be more rigorous for modeling aggregation of this mAb at this temperature condition, future work will need to include a longer-term stability study to mechanistically examine mAb aggregation at lower temperatures and to test the applicability of these models to predict protein storage life under lower temperature conditions. Thus, although the results at 25 °C do not show any appreciable differences in their modeled rate constants, the data should not be over interpreted due to the lack of an apparent characteristic time scale observed in the monomer loss vs time data.

The Effect of the Physical Properties of the mAb in Different Solutions on Modeled Aggregate Nucleation and Growth Values. When taken together, the two simulated aggregation rate constants modeled from the mAb stability data in various solution and temperature conditions provide several important results in terms of better understanding the aggregation mechanism of experimental data in relation to the physical properties of the mAb. To this end, as shown in Figure 6A, the modeled values of $k_{nuc,obs}$ (mAb aggregation observed nucleation rate constants) are presented as a function of apparent melting temperature (T_m values from DSC measurements; see Table 1) minus incubation storage temperature (T) for all of the examined storage and solution conditions. This temperature scale of ($T_m - T$) was used to better evaluate the effect of partially unfolded mAb on the observed aggregation nucleation rate constants. The modeled nucleation rate constants were normalized by the smallest value to observe differences between the solution and temperature conditions on a relative scale (also, it should be noted that for this analysis aggregation data for pH 6.5 mAb samples incubated at 57 °C, and for mAb samples incubated at 25 °C, are not included because of the limitations outlined in the previous sections).

At 40 °C incubation ($T_m - T$ ranging from ~15 to 20 °C in Figure 6A), the observed nucleation rate constants for the mAb in pH 4.5 histidine (dark red), pH 4.5 histidine + NaCl (light red), pH 4.5 citrate (dark blue), and pH 4.5 citrate + NaCl (light blue) solutions appear to be similar and randomly distributed. Interestingly, differences in a_2 or the apparent solubility profiles (e.g., midpoint or extrapolated activity values, Table 2) were not reflected in the modeled $k_{nuc,obs}$ values for solution conditions with similar $T_m - T$ values (Figure 6A). At 57 °C incubation ($T_m - T < 5$ °C), the modeled nucleation rates increased rapidly as $T_m - T$ decreased. This seems

DOI: 10.1021/acs.jpcb.6b03878
J. Phys. Chem. B 2016, 120, 7062−7075

intuitive because the nucleation mechanism, expected to be fastest at high temperatures, has an observed rate constant which scales with the fraction of unfolded protein squared. It was unexpected, however, that the colloidal environment in the different solution conditions did not appear to have any affect the observed nucleation rate constants, since we had originally hypothesized that conformationally altered proteins were more likely to stick upon collisions and would therefore appear to follow the theory of slow coagulation (see eq 2).

In the context of this model, this result from Figure 6A implies that the process of aggregate nucleation for this mAb behaves similarly to limiting case 2 as presented in the Theoretical Role of Colloidal Stability on Aggregation Rates section. In other words, structural alterations of associated mAb monomers to form a stable irreversible mAb dimer could be the rate limiting component of aggregate nucleation. Additionally, we did not observe any apparent correlation of the experimental aggregation rate in different solutions to the apparent solubility values of the mAb in the same solutions (as measured in PEG precipitation assay). This is probably because partially unfolded intermediates of the mAb would be expected to have lower solubility values. If the equilibrium association constant is high for the mAb in every solution, then we would expect only conformational rearrangement of an encounter complex to be the rate limiting step. In this study, the nucleation mechanism involving encounter complex formation between native mAb molecules, described by eq 3c, did not appear to be a major pathway for this mAb. It would be interesting to see in future work if nucleation of other mAb molecules, which undergo that pathway to a greater extent, correlates with such apparent solubility measurements as seen previously by others with using different mAbs.[22,23]

Using the same approach described above, the modeled values of $k_{g,obs}$ (observed growth rate constants for mAb aggregation) are presented as a function $T_m - T$ to better observe the role of conformational changes (i.e., CH_2 domain unfolding as seen by DSC) on growth processes during aggregation of this mAb (Figure 6B). In contrast to Figure 6A, it is readily apparent in Figure 6B that the correlation is not as strong between mAb aggregate growth and the relative concentration of partially unfolded mAb as approximately given by $T_m - T$. One potential explanation is that the observed growth rate constants (Figure 6B) were more sensitive to the colloidal environment of the mAb as measured by a_2 and PEG precipitation values (Table 2). The deviations between $k_{g,obs}$ values for the mAb in different solution environments, but at similar $T_m - T$ values, appear to best correlate with the rank ordering of the apparent solubility profiles for the native mAb in different solutions (Figure 3c). Furthermore, it is difficult to physically justify how encounter complex formation could be rate limiting at the relatively low a_2 values observed in this study. Therefore, although we conclude that aggregate growth by monomer addition was sensitive to the colloidal environment of the mAb under these conditions, we suspect that rates were affected by association thermodynamics rather than kinetics. In other words, based on these considerations, it is reasonable to conclude that similar to aggregate nucleation, aggregate growth also follows limiting case 2 as presented in the Theory—Role of Colloidal Stability and Apparent Solubility on Aggregation Rates section. Except that in this case, it was probably the equilibrium concentration of associated encounter complex that was rate limiting rather than the structural rearrangement of the encounter complex. For example, although there was substantial monomer loss in the pH 4.5 mAb sample in histidine buffer incubated at 57 °C for 3 days, there was limited aggregate growth. Note that this solution condition had the highest solubility in PEG solutions compared to the other mAb solution conditions. Barnett et al. previously rationalized this type of observation by arguing that when protein−protein interactions are strongly repulsive, a monomer diffusing toward an aggregate would be felt simultaneously by all of the monomeric components within the aggregate causing extensive growth to become highly unfavorable.[59]

CONCLUSIONS

In this study we evaluated the aggregation vs storage time profile of an IgG1 mAb under different solution conditions across a range of temperatures by SEC or SV-AUC, and compared results to the physical properties of the mAb in different solutions including partially unfolded intermediates (conformational stability by DSC), apparent solubility (in PEG solutions), and protein−protein interactions (second virial coefficients by SLS). A kinetic model for aggregation was developed and applied to interpret SEC and SV-AUC aggregation data during storage of the IgG1 mAb at different temperatures in terms of the roles of aggregate nucleation and growth. Additional kinetic equations describing the effects of conformational stability, colloidal stability, and equilibrium encounter complex formation were also proposed.

We found that the modeled nucleation rate constants for aggregation of this mAb in different solutions were most sensitive to the formation of partially unfolded intermediates (i.e., conformational stability of the mAb). In other words, as the incubation temperature approached the thermal melting temperature (as measured by DSC), the observed aggregation nucleation increased as expected. Interestingly, the observed aggregation nucleation rate constants did not appear to be affected by protein−protein interactions and/or apparent solubility values for this mAb under these various solution and temperature conditions. As a result, we conclude that the association processes between protein monomers were not a rate limiting step of aggregate nucleation for this mAb under these solution and storage conditions.

On the other hand, aggregate growth rate constants (by monomer addition) for this mAb in the same solutions were highly sensitive to protein−protein interactions and/or apparent solubility values (i.e., association thermodynamics) as well as to the conformational stability (i.e., concentration of partially unfolded intermediates) when the mAb was incubated at 57 and 40 °C. Based on the relatively low values of a_2 measured in this study, it is difficult to physically justify long-range repulsive interactions causing the rate of protein associations to become the rate limiting step; thus, it is more likely that the thermodynamics of encounter complex formation of the mAb in the different solutions was the rate limiting component of aggregate growth in the same solutions during storage. Thus, this work provides a method to model experimentally obtained protein aggregation stability data to enable a better mechanistic understanding of the relative contributions of nucleation and growth components of the aggregation pathway as a function of solution conditions and temperature for proteins of interest.

DOI: 10.1021/acs.jpcb.6b03878
J. Phys. Chem. B 2016, 120, 7062−7075

■ ASSOCIATED CONTENT

Supporting Information

The Supporting Information is available free of charge on the ACS Publications website at DOI: 10.1021/acs.jpcb.6b03878.

Subvisible protein particle data measured using flow microscopy and additional discussion of assumptions made for kinetic modeling (PDF)

■ AUTHOR INFORMATION

Corresponding Author

*Telephone: 301-975-6847; Fax: 301-975-4924; Email: cavan.kalonia@nist.gov.

Present Addresses

‡National Institute of Standards and Technology, Gaithersburg, MD 20899

§University of Colorado Denver, Aurora, CO 80045

Notes

The authors declare no competing financial interest.

■ ACKNOWLEDGMENTS

The authors wish to thank and acknowledge Professor Christopher Roberts, University of Delaware, for his thoughtful comments and critical review of this manuscript and Dr. Aaron Smalter Hall at the University of Kansas for developing the simulation script. Janssen R&D is acknowledged for providing the IgG1 mAb for this study and Fluid Imaging Technologies for providing a VS series FlowCam instrument for flow microscopy measurements. Financial support is acknowledged from NIH biotechnology training grant 5-T32-GM008359 (Cavan Kalonia).

■ REFERENCES

(1) Philo, J. S.; Arakawa, T. Mechanisms of Protein Aggregation. *Curr. Pharm. Biotechnol.* **2009**, *10*, 348−51.

(2) Amin, S.; Barnett, G. V.; Pathak, J. A.; Roberts, C. J.; Sarangapani, P. S. Protein Aggregation, Particle Formation, Characterization & Rheology. *Curr. Opin. Colloid Interface Sci.* **2014**, *19*, 438−449.

(3) Roberts, C. J., Nucleation, Aggregation, and Conformational Distortion. In *Biophysical Methods for Biotherapeutics: Discovery and Development Applications*, First ed.; Das, T. K., Ed.; John Wiley & Sons, Inc: Hoboken, NJ, 2014; pp 125−144.

(4) Rosenberg, A. S. Effects of Protein Aggregates: An Immunologic Perspective. *AAPS J.* **2006**, *8*, E501−7.

(5) Ratanji, K. D.; Derrick, J. P.; Dearman, R. J.; Kimber, I. Immunogenicity of Therapeutic Proteins: Influence of Aggregation. *J. Immunotoxicol.* **2014**, *11*, 99−109.

(6) Carpenter, J. F.; et al. Overlooking Subvisible Particles in Therapeutic Protein Products: Gaps That May Compromise Product Quality. *J. Pharm. Sci.* **2009**, *98*, 1201−5.

(7) Joubert, M. K.; et al. Highly Aggregated Antibody Therapeutics Can Enhance the in Vitro Innate and Late-Stage T-Cell Immune Responses. *J. Biol. Chem.* **2012**, *287*, 25266−25279.

(8) Bi, V.; et al. Development of a Human Antibody Tolerant Mouse Model to Assess the Immunogenicity Risk Due to Aggregated Biotherapeutics. *J. Pharm. Sci.* **2013**, *102*, 3545−55.

(9) Shankar, G.; Shores, E.; Wagner, C.; Mire-Sluis, A. Scientific and Regulatory Considerations on the Immunogenicity of Biologics. *Trends Biotechnol.* **2006**, *24*, 274−80.

(10) Telikepalli, S.; Shinogle, H. E.; Thapa, P. S.; Kim, J. H.; Deshpande, M.; Jawa, V.; Middaugh, C. R.; Narhi, L. O.; Joubert, M. K.; Volkin, D. B. Physical Characterization and in Vitro Biological Impact of Highly Aggregated Antibodies Separated into Size-Enriched Populations by Fluorescence-Activated Cell Sorting. *J. Pharm. Sci.* **2015**, *104*, 1575−1591.

(11) Joubert, M. K.; Luo, Q.; Nashed-Samuel, Y.; Wypych, J.; Narhi, L. O. Classification and Characterization of Therapeutic Antibody Aggregates. *J. Biol. Chem.* **2011**, *286*, 25118−33.

(12) Chennamsetty, N.; Voynov, V.; Kayser, V.; Helk, B.; Trout, B. L. Prediction of Aggregation Prone Regions of Therapeutic Proteins. *J. Phys. Chem. B* **2010**, *114*, 6614−24.

(13) Neudecker, P.; Robustelli, P.; Cavalli, A.; Walsh, P.; Lundstrom, P.; Zarrine-Afsar, A.; Sharpe, S.; Vendruscolo, M.; Kay, L. E. Structure of an Intermediate State in Protein Folding and Aggregation. *Science* **2012**, *336*, 362−6.

(14) Baynes, B. M.; Trout, B. L. Rational Design of Solution Additives for the Prevention of Protein Aggregation. *Biophys. J.* **2004**, *87*, 1631−9.

(15) Baynes, B. M.; Wang, D. I.; Trout, B. L. Role of Arginine in the Stabilization of Proteins against Aggregation. *Biochemistry* **2005**, *44*, 4919−25.

(16) Kalonia, C.; Kumru, O. S.; Kim, J. H.; Middaugh, C. R.; Volkin, D. B. Radar Chart Array Analysis to Visualize Effects of Formulation Variables on Igg1 Particle Formation as Measured by Multiple Analytical Techniques. *J. Pharm. Sci.* **2013**, *102*, 4256−67.

(17) Telikepalli, S. N.; Kumru, O. S.; Kalonia, C.; Esfandiary, R.; Joshi, S. B.; Middaugh, C. R.; Volkin, D. B. Structural Characterization of Igg1Mab Aggregates and Particles Generated under Various Stress Conditions. *J. Pharm. Sci.* **2014**, *103*, 796−809.

(18) Bee, J. S.; Schwartz, D. K.; Trabelsi, S.; Freund, E.; Stevenson, J. L.; Carpenter, J. F.; Randolph, T. W. Production of Particles of Therapeutic Proteins at the Air−Water Interface During Compression/Dilation Cycles. *Soft Matter* **2012**, *8*, 10329−10335.

(19) Roberts, C. J.; Das, T. K.; Sahin, E. Predicting Solution Aggregation Rates for Therapeutic Proteins: Approaches and Challenges. *Int. J. Pharm.* **2011**, *418*, 318−33.

(20) Kamerzell, T. J.; Esfandiary, R.; Joshi, S. B.; Middaugh, C. R.; Volkin, D. B. Protein-Excipient Interactions: Mechanisms and Biophysical Characterization Applied to Protein Formulation Development. *Adv. Drug Delivery Rev.* **2011**, *63*, 1118−1159.

(21) Chi, E. Y.; Krishnan, S.; Randolph, T. W.; Carpenter, J. F. Physical Stability of Proteins in Aqueous Solution: Mechanism and Driving Forces in Nonnative Protein Aggregation. *Pharm. Res.* **2003**, *20*, 1325−36.

(22) Banks, D. D.; Latypov, R. F.; Ketchem, R. R.; Woodard, J.; Scavezze, J. L.; Siska, C. C.; Razinkov, V. I. Native-State Solubility and Transfer Free Energy as Predictive Tools for Selecting Excipients to Include in Protein Formulation Development Studies. *J. Pharm. Sci.* **2012**, *101*, 2720−32.

(23) Banks, D. D.; Zhang, J.; Siska, C. C. Relationship between Native-State Solubility and Non-Native Aggregation of Recombinant Human Granulocyte Colony Stimulating Factor: Practical Implications for Protein Therapeutic Development. *Mol. Pharmaceutics* **2014**, *11*, 3431−3442.

(24) Gibson, T. J.; McCarty, K.; McFadyen, I. J.; Cash, E.; Dalmonte, P.; Hinds, K. D.; Dinerman, A. A.; Alvarez, J. C.; Volkin, D. B. Application of a High-Throughput Screening Procedure with Peg-Induced Precipitation to Compare Relative Protein Solubility During Formulation Development with Igg1Monoclonal Antibodies. *J. Pharm. Sci.* **2011**, *100*, 1009−21.

(25) Middaugh, C. R.; Tisel, W. A.; Haire, R. N.; Rosenberg, A. Determination of the Apparent Thermodynamic Activities of Saturated Protein Solutions. *J. Biol. Chem.* **1979**, *254*, 367−370.

(26) Zhang, J. Protein-Protein Interactions in Salt Solutions. In *Protein-Protein Interactions -Computational and Experimental Tools*, Cal, W., Hong, H., Eds.; Intech, 2012.

(27) Saluja, A.; Kalonia, D. S. Nature and Consequences of Protein-Protein Interactions in High Protein Concentration Solutions. *Int. J. Pharm.* **2008**, *358*, 1−15.

(28) Mcmillan, W. G.; Mayer, J. E. The Statistical Thermodynamics of Multicomponent Systems. *J. Chem. Phys.* **1945**, *13*, 276−305.

(29) Siderius, D. W.; Krekelberg, W. P.; Roberts, C. J.; Shen, V. K. Osmotic Virial Coefficients for Model Protein and Colloidal Solutions:

DOI: 10.1021/acs.jpcb.6b03878
J. Phys. Chem. B 2016, 120, 7062−7075

Importance of Ensemble Constraints in the Analysis of Light Scattering Data. *J. Chem. Phys.* **2012**, *136*, 175102.
(30) Curtis, R. A.; Montaser, A.; Prausnitz, J. M.; Blanch, H. W. Protein-Protein and Protein-Salt Interactions in Aqueous Protein Solutions Containing Concentrated Electrolytes. *Biotechnol. Bioeng.* **1998**, *58*, 451.
(31) Hiemenz, P. C.; Rajagopalan, R. *Principles of Colloid and Surface Chemistry*, 3rd ed.; Marcel Dekker, Inc.: New York, 1997.
(32) Bajaj, H.; Sharma, V. K.; Badkar, A.; Zeng, D.; Nema, S.; Kalonia, D. S. Protein Structural Conformation and Not Second Virial Coefficient Relates to Long-Term Irreversible Aggregation of a Monoclonal Antibody and Ovalbumin in Solution. *Pharm. Res.* **2006**, *23*, 1382−94.
(33) Sahin, E.; Grillo, A. O.; Perkins, M. D.; Roberts, C. J. Comparative Effects of Ph and Ionic Strength on Protein-Protein Interactions, Unfolding, and Aggregation for Igg1 Antibodies. *J. Pharm. Sci.* **2010**, *99*, 4830−48.
(34) Li, Y.; Roberts, C. J. Lumry-Eyring Nucleated-Polymerization Model of Protein Aggregation Kinetics. 2. Competing Growth Via Condensation and Chain Polymerization. *J. Phys. Chem. B* **2009**, *113*, 7020−32.
(35) Andrews, J. M.; Roberts, C. J. A Lumry-Eyring Nucleated Polymerization Model of Protein Aggregation Kinetics: 1. Aggregation with Pre-Equilibrated Unfolding. *J. Phys. Chem. B* **2007**, *111*, 7897−913.
(36) Ghazvini, S.; Kalonia, C.; Volkin, D. B.; Dhar, P. Evaluating the Role of the Air-Solution Interface on the Mechanism of Subvisible Particle Formation Caused by Mechanical Agitation for an Igg1Mab. *J. Pharm. Sci.* **2016**, *105*, 1643.
(37) Bond, M. D.; et al. Evaluation of a Dual-Wavelength Size Exclusion Hplc Method with Improved Sensitivity to Detect Protein Aggregates and Its Use to Better Characterize Degradation Pathways of an Igg1Monoclonal Antibody. *J. Pharm. Sci.* **2010**, *99*, 2582−97.
(38) Schuck, P. Size-Distribution Analysis of Macromolecules by Sedimentation Velocity Ultracentrifugation and Lamm Equation Modeling. *Biophys. J.* **2000**, *78*, 1606−19.
(39) Wyatt, P. J. Light-Scattering and the Absolute Characterization of Macromolecules. *Anal. Chim. Acta* **1993**, *272*, 1−40.
(40) Harding, S. E.; Horton, J. C.; Jones, S.; Thornton, J. M.; Winzor, D. J. Covol: An Interactive Program for Evaluating Second Virial Coefficients from the Triaxial Shape or Dimensions of Rigid Macromolecules. *Biophys. J.* **1999**, *76*, 2432−2438.
(41) DeLano, W. L.; Lam, J. W. Pymol: A Communications Tool for Computational Models. *Abstr Pap Am. Chem. S.* 2005; Vol. *230*, pp U1371−U1372
(42) Padlan, E. A. Anatomy of the Antibody Molecule. *Mol. Immunol.* **1994**, *31*, 169−217.
(43) Sali, A.; Blundell, T. L. Comparative Protein Modeling by Satisfaction of Spatial Restraints. *J. Mol. Biol.* **1993**, *234*, 779−815.
(44) Matsumiya, S.; Yamaguchi, Y.; Saito, J.; Nagano, M.; Sasakawa, H.; Otaki, S.; Satoh, M.; Shitara, K.; Kato, K. Structural Comparison of Fucosylated and Nonfucosylated Fc Fragments of Human Immunoglobulin G1. *J. Mol. Biol.* **2007**, *368*, 767−779.
(45) Olsson, M. H. M.; Sondergaard, C. R.; Rostkowski, M.; Jensen, J. H. Propka3: Consistent Treatment of Internal and Surface Residues in Empirical Pk(a) Predictions. *J. Chem. Theory Comput.* **2011**, *7*, 525−537.
(46) Li, H.; Robertson, A. D.; Jensen, J. H. Very Fast Empirical Prediction and Rationalization of Protein Pk(a) Values. *Proteins: Struct., Funct., Genet.* **2005**, *61*, 704−721.
(47) Vermeer, A. W. P.; Norde, W. The Thermal Stability of Immunoglobulin: Unfolding and Aggregation of a Multi-Domain Protein. *Biophys. J.* **2000**, *78*, 394−404.
(48) Vermeer, A. W. P.; Norde, W.; van Amerongen, A. The Unfolding/Denaturation of Immunogammaglobulin of Isotype 2b and Its F-Ab and F-C Fragments. *Biophys. J.* **2000**, *79*, 2150−2154.
(49) Ionescu, R. M.; Vlasak, J.; Price, C.; Kirchmeier, M. Contribution of Variable Domains to the Stability of Humanized Igg1Monoclonal Antibodies. *J. Pharm. Sci.* **2008**, *97*, 1414−1426.
(50) Sanchezruiz, J. M. Theoretical-Analysis of Lumry-Eyring Models in Differential Scanning Calorimetry. *Biophys. J.* **1992**, *61*, 921−935.
(51) Mahadevan, H.; Hall, C. K. Statistical-Mechanical Model of Protein Precipitation by Nonionic Polymer. *AIChE J.* **1990**, *36*, 1517−1528.
(52) Asakura, S.; Oosawa, F. On Interaction between 2 Bodies Immersed in a Solution of Macromolecules. *J. Chem. Phys.* **1954**, *22*, 1255−1256.
(53) Asakura, S.; Oosawa, F. Interaction between Particles Suspended in Solutions of Macromolecules. *J. Polym. Sci.* **1958**, *33*, 183−192.
(54) Sarangapani, P. S.; Hudson, S. D.; Jones, R. L.; Douglas, J. F.; Pathak, J. A. Critical Examination of the Colloidal Particle Model of Globular Proteins. *Biophys. J.* **2015**, *108*, 724−737.
(55) Dumetz, A. C.; Snellinger-O'Brien, A. M.; Kaler, E. W.; Lenhoff, A. M. Patterns of Protein - Protein Interactions in Salt Solutions and Implications for Protein Crystallization. *Protein Sci.* **2007**, *16*, 1867−1877.
(56) Asthagiri, D.; Paliwal, A.; Abras, D.; Lenhoff, A. M.; Paulaitis, M. E. A Consistent Experimental and Modeling Approach to Light-Scattering Studies of Protein-Protein Interactions in Solution. *Biophys. J.* **2005**, *88*, 3300−3309.
(57) Blanco, M. A.; Sahin, E.; Li, Y.; Roberts, C. J. Reexamining Protein-Protein and Protein-Solvent Interactions from Kirkwood-Buff Analysis of Light Scattering in Multi-Component Solutions. *J. Chem. Phys.* **2011**, *134*, 225103.
(58) Blanco, M. A.; Perevozchikova, T.; Martorana, V.; Manno, M.; Roberts, C. J. Protein-Protein Interactions in Dilute to Concentrated Solutions: Alpha-Chymotrypsinogen in Acidic Conditions. *J. Phys. Chem. B* **2014**, *118*, 5817−5831.
(59) Barnett, G. V.; Razinkov, V. I.; Kerwin, B. A.; Laue, T. M.; Woodka, A. H.; Butler, P. D.; Perevozchikova, T.; Roberts, C. J. Specific-Ion Effects on the Aggregation Mechanisms and Protein-Protein Interactions for Anti-Streptavidin Immunoglobulin Gamma-1. *J. Phys. Chem. B* **2015**, *119*, 5793−5804.
(60) Minton, A. P. Static Light Scattering from Concentrated Protein Solutions, I: General Theory for Protein Mixtures and Application to Self-Associating Proteins. *Biophys. J.* **2007**, *93*, 1321−1328.
(61) Bonnete, F.; Vivares, D. Interest of the Normalized Second Virial Coefficient and Interaction Potentials for Crystallizing Large Macromolecules. *Acta Crystallogr., Sect. D: Biol. Crystallogr.* **2002**, *58*, 1571−1575.
(62) Dumetz, A. C.; Chockla, A. M.; Kaler, E. W.; Lenhoff, A. M. Effects of Ph on Protein-Protein Interactions and Implications for Protein Phase Behavior. *Biochim. Biophys. Acta, Proteins Proteomics* **2008**, *1784*, 600−610.

DOI: 10.1021/acs.jpcb.6b03878
J. Phys. Chem. B 2016, 120, 7062−7075